

Accurate prediction of thermal conductivity of Al_2O_3 at ultrahigh temperatures

Janak Tiwari  and Tianli Feng ^{*}

Department of Mechanical Engineering, University of Utah, Salt Lake City, Utah 84112, USA



(Received 13 December 2023; revised 24 January 2024; accepted 25 January 2024; published 13 February 2024)

Many complex crystals show a flat or even increasing lattice thermal conductivity at high temperatures, which deviates from the traditional $1/T$ decay trend given by conventional phonon theory. In this paper, we predict the thermal conductivity of Al_2O_3 that matches with experimental data from room temperature to near melting point (2200 K). The lattice thermal conductivity is found to be composed of contributions of phonon, diffuson, and radiation. Phonon particle thermal conductivity decays approximately as $\sim T^{-1.14}$ after considering four-phonon (4ph) scattering as well as finite-temperature corrections to the lattice constant and harmonic and anharmonic force constants (AFCs). Diffuson (interband tunneling) thermal conductivity increases roughly as $\sim T^{0.43}$. Radiation thermal conductivity increases as $\sim T^{2.51}$, being slightly smaller than $\sim T^3$ due to the increase of phonon linewidth with temperature, which increases photon extinction coefficient and reduces photon mean free path (MFP). At room temperature, phonon, diffuson, and radiation contribute ~ 99 , 1 , and 0% , respectively. At 2200 K, their contributions change to 61 , 20 , and 19% , respectively. 4ph scattering is important at ultrahigh temperatures, decreasing the phonon thermal conductivity by a maximum of 24% . The finite-temperature softening effects of the harmonic and AFCs increase the phonon thermal conductivity by a maximum of 36% at ultrahigh temperatures. We also verify that Green-Kubo molecular dynamics can capture both the particle and wave nature of phonons, like the Wigner formalism. At ultrahigh temperatures, the photon MFP is found to be on the order of 100 nm, which should be considered for experimental measurement of thin films. In this paper, we aim to enhance the understanding of lattice thermal conductivity in complex crystals at ultrahigh temperatures, potentially spurring further exploration of materials suitable for such extreme conditions.

DOI: [10.1103/PhysRevB.109.075201](https://doi.org/10.1103/PhysRevB.109.075201)

I. INTRODUCTION

Thermal conductivity of complex crystals at high temperatures is critical for many applications, such as thermal barrier coatings [1,2], refractory materials [3,4], crucibles, and high-temperature thermal insulation [5,6]. However, current state-of-the-art theoretical prediction based on the phonon-gas model (PGM) [7–9] could not explain their intriguing thermal conductivity (κ). At intermediate temperatures, κ decays with temperature (T), being consistent with typical crystal behavior. However, at high temperatures, κ either increases or remains independent of temperature, displaying a peculiar and anomalous glasslike behavior. While the former behavior can be explained using PGM based on the Boltzmann transport equation (BTE), which primarily involves three-phonon (3ph) or four-phonon (4ph) scattering processes, the latter phenomenon remains a puzzle, presenting an unanswered question.

In this paper, we take Al_2O_3 as an example to investigate the flattening or increasing trend of thermal conductivity at high temperatures for the following reasons. (1) Al_2O_3 has excellent mechanical strength, high-temperature thermal and chemical stability [10–12], large band gap [13], high dielectric constant [14], high melting point [15], and is widely used in many high-temperature engineering applications. (2) It does

not have an electronic contribution to heat transfer, leaving the theoretical lattice thermal conductivity readily comparable with experimental data. (3) It can be grown to a large-sized single crystal with high purity, so grain boundary and defect scattering can be neglected. (4) Extensive experimental data [16–25] are available to validate our study.

In this paper, we investigate several possible improvements to the current state-of-the-art κ prediction to explain the flattening or increasing trend of thermal conductivity in complex crystals at ultrahigh temperatures. One improvement is the temperature correction on lattice structure and phonon-phonon scattering. The current phonon theory relies on the ground-state lattice structure and force constant, where 3ph \propto phonon population (n) $\propto T$ and 4ph $\propto n^2 \propto T^2$ [26,27], resulting in phonon thermal conductivity (κ_{ph}) decay with power law T^{-1} and T^{-2} , respectively, for 3ph and 4ph scattering. However, phonon renormalization at high temperatures due to lattice expansion and temperature dependence of harmonic force constant changes 3ph and 4ph scattering phase space [28], which may lead to an increase in κ_{ph} . Recently, it has been reported that the temperature dependence of the anharmonic force constant (AFC) reduces the scattering probability (or scattering cross-section) [28,29], which increases κ_{ph} . These make the thermal conductivity flatter at higher temperatures compared with ground-state calculations.

The second improvement could be the incorporation of the diffuson thermal conductivity (κ_{dif} or κ_c) along with κ_{ph} . In PGM and BTE, the primary heat carriers are propagating

^{*}tianli.feng@utah.edu

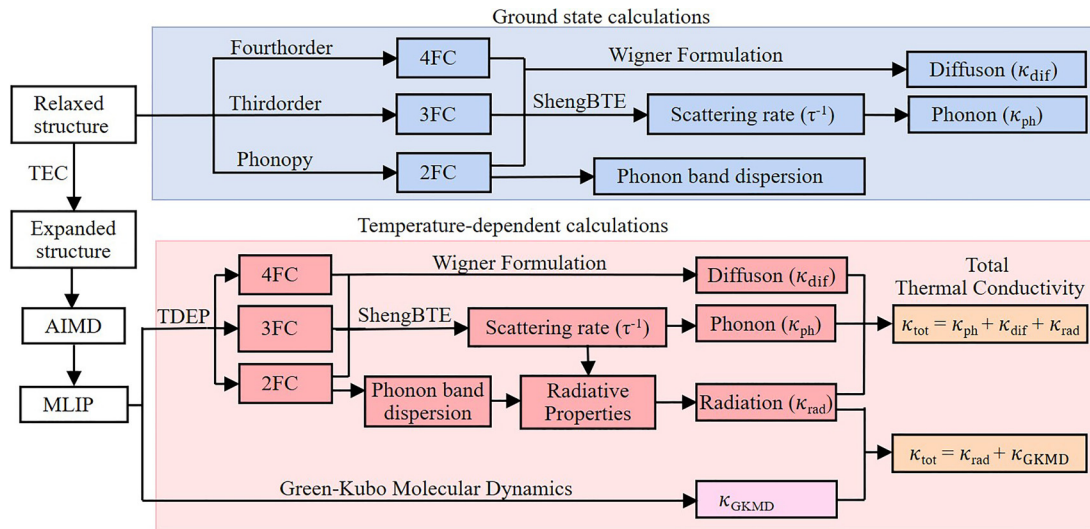


FIG. 1. Computation workflow of the study.

phonons (particlelike phonons), which account only for the diagonal terms of the velocity operator. This is a good approximation for simple crystals [30], where the phonon branches are well separated, i.e., interband spacings are much larger than the phonon linewidths. However, this approximation fails in the complex crystals and disordered regime [31], where phonon bands are not well separated, and many phonon modes might overlap with each other. In this scenario, phonons show wavelike transport properties, i.e., they can tunnel from one mode into another and conduct heat. Recently, Simoncelli *et al.* [32,33] introduced the Wigner transport equation which encompasses particlelike and wavelike conduction mechanisms, providing a unified approach to the heat-transport phenomena in solids, including simple crystals (where particlelike propagation dominates), glasses (where wavelike tunneling or diffusons dominates), and all intermediate cases (complex crystals where both particlelike and wavelike conduction mechanisms coexist). The significant κ_{dif} is reported for many complex crystals [34–37] and used to explain the flattening of κ at higher temperatures.

The temperature effect on both κ_{ph} and κ_{dif} could also be studied using molecular dynamics (MD) simulations. In principle, MD should capture all orders of phonon-phonon interaction as well as diffuson, due to its ability to simulate the intricate behavior of individual atoms, thereby capturing all the underlying microscopic mechanisms governing lattice heat transfer. MD, while powerful, is limited by the accuracy of the interatomic potential functions they rely on. Classical potentials, based on empirical models, often involve approximations and force field parameters, leading to inherent inaccuracies in capturing the complex quantum mechanical behaviors of atoms and molecules. Machine-learning interatomic potentials (MLIPs), on the other hand, have very high accuracy, comparable with that of density functional theory (DFT) calculations. In this paper, we train the moment tensor potential (MTP) [38–40] from *ab initio* MD (AIMD) snapshots and use it to run Green-Kubo MD (GKMD) [41,42] to calculate thermal conductivity (κ_{GKMD}).

The third improvement could be the incorporation of radiation thermal conduction (κ_{rad}) to overall thermal conductivity.

Like phonons, photons also propagate inside and through the crystal and transport the heat, which contributes to apparent thermal conductivity. Radiation contribution has been hypothesized as a primary reason for the increase in thermal conductivity at ultrahigh temperatures in early literature [18,21,24,43–46]. However, the radiation thermal conductivity has not been calculated rigorously from first principles. Here, we calculate the radiative properties using the Lorentz oscillator model [47,48] and estimate the radiation thermal conductivity based on the Rosseland model.

In this paper, we present the thermal transport of Al_2O_3 from room temperature to the melting point (2200 K) by incorporating the temperature-dependent force constants in κ_{ph} calculation and considering κ_{dif} and κ_{rad} . Here, κ_{ph} and κ_{dif} contributions are calculated using Wigner formalism and GKMD separately. The remaining sections of the paper are structured as follows. In Sec. II, we present the computations details and methodology used in the study. Sections III and IV present the main results and discussions, respectively. Finally, Sec. V presents the conclusions.

II. METHODOLOGY

A. Computational workflow

Figure 1 shows the computational workflow of the study. First, the structure is relaxed by using VASP [49,50], using generalized gradient approximation [51] method and the Perdew-Burke-Ernzerhof functional revised for solids (PBEsol) [52]. The plane-energy cutoff used in the calculations is 500 eV, and the energy and force convergence thresholds are 1×10^{-8} eV and 1×10^{-7} eV \AA^{-1} , respectively. Al_2O_3 belongs to the trigonal lattice structure system (space group $R\bar{3}c$), with a rhombohedral primitive unit cell containing 10 atoms. The relaxed lattice parameters are $a = 5.139$ \AA and $\alpha = 55.35^\circ$, which closely resemble the experimental values [53,54] of $a = 5.128$ \AA and $\alpha = 55.28^\circ$. In DFT calculations, supercells of $3 \times 3 \times 3$ (270 atoms) are used with a \mathbf{k} -point grid of $4 \times 4 \times 4$. Other parameters are kept constant as that of relaxation.

For the ground-state calculations, harmonic or second-order force constants (2FCs) are extracted using PHONOPY [55] considering the fourth-nearest neighbors. The AFCs, including third-order force constants (3FCs) and fourth-order force constants (4FCs), are calculated using the THIRDORDER and FOURTHORDER packages built inside ShengBTE [56], considering the fourth and second nearest atoms, respectively. For the finite-temperature calculations, the structure is expanded using the thermal expansion coefficient (TEC). The AIMD is computed, and snapshots are recorded, from which the MTP-based [39,40,57] MLIP is trained. GKMD is performed by using the MLIP-LAMMPS package [39,58] to calculate κ_{GKMD} . The temperature-dependent harmonic and AFCs are extracted using the temperature-dependent effective potential (TDEP) method [59,60]. Using the force constants, κ_{ph} and κ_{dif} are calculated by solving Wigner's formalism [32,33] under ShengBTE. Radiative properties are calculated using the Lorentz oscillator model, from which κ_{rad} is calculated using the Rooseland model. Finally, the total thermal conductivity (κ_{tot} or κ) is calculated by summing up κ_{ph} , κ_{dif} , and κ_{rad} as well as κ_{GKMD} and κ_{rad} separately. The details of each step are explained below.

B. TEC

The linear TEC is calculated using quasiharmonic approximation (QHA) with the following formalism [61]:

$$\alpha_L = -\frac{k_B}{3N_{\mathbf{q}}V_c B} \sum_{\mathbf{q},j} \gamma_{\mathbf{q},j} \cdot \left(\frac{x}{2}\right)^2 \cdot \left[1 - \coth^2\left(\frac{x}{2}\right)\right].$$

Here, (\mathbf{q}, j) stands for a phonon mode with wave vector \mathbf{q} and dispersion branch j . Also, $N_{\mathbf{q}}$ is the number of phonon \mathbf{q} points, V_c is the volume of a primitive cell of Al_2O_3 , k_B is the Boltzmann constant, and $B = -V \frac{dP}{dV}$ is the bulk modulus. The summation is done over all the $3N_{\mathbf{q}}n_b$ phonon modes, where n_b is the number of basis atoms in a primitive cell. Here, x is short for $x = \hbar\omega_{\mathbf{q},j}/k_B T$, and $\gamma_{\mathbf{q},j} = -\frac{V}{\omega_{\mathbf{q},j}} \frac{\partial \omega_{\mathbf{q},j}}{\partial V}$ is the mode-dependent Grüneisen parameter. In this paper, an $18 \times 18 \times 18$ \mathbf{q} -mesh is used in the TEC calculations.

The bulk modulus at the ground state is calculated using VASP by the finite difference method using $B = -V \frac{dP}{dV}$, which gives $B = 249$ GPa. It matches well with the experimental data of 248.7 GPa [62] and 257 GPa [17]. The Grüneisen parameters are obtained by two methods. One is using the finite difference method, based on the definition of $\gamma_{\mathbf{q},j} = -\frac{V}{\omega_{\mathbf{q},j}} \frac{\partial \omega_{\mathbf{q},j}}{\partial V}$, implemented in PHONOPY [55]. The other method is to use the third-order AFC to predict γ_{λ} as implemented in ShengBTE [56]. As shown in Fig. 2, the predicted TEC using the ground-state bulk modulus (blue-dashed curve with Grüneisen parameter from PHONOPY and black-dashed curves with Grüneisen parameter from ShengBTE) match experimental data at low to medium temperatures but deviates at ultrahigh temperatures. This deviation has been reported to be corrected by using the temperature-dependent bulk modulus [28]. With the temperature-dependent bulk modulus [17], the predicted TEC agrees with experimental data even at ultrahigh temperatures [17,64,65]. QHA generally tends to overestimate thermal expansivity at high temperatures, which has been attributed to anharmonicity at high temperatures [66,67].

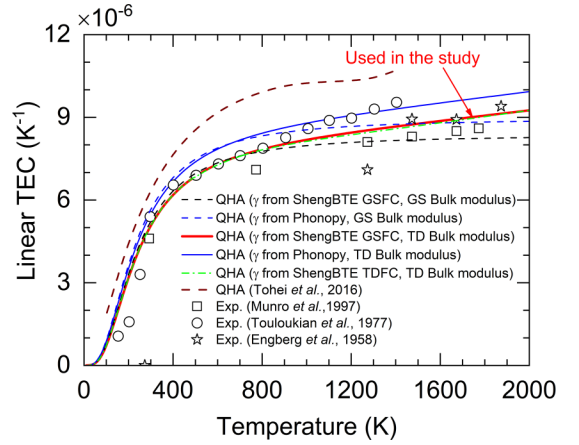


FIG. 2. Linear thermal expansion coefficient (TEC) of Al_2O_3 as a function of temperature. The theoretical TEC (lines) are calculated by quasiharmonic approximation (QHA) using the Grüneisen parameter and bulk modulus obtained from different ways. The ground state (GS) bulk modulus is calculated by density functional theory (DFT), and temperature-dependent (TD) bulk modulus is taken from Ref. [17]. The DFT predicted data by Tohei *et al.* [63] and different experimental data [17,64,65] are included for comparison.

This deviation could be corrected by the phonon quasiparticle approach [68,69] or accurate calculation of mode Grüneisen parameters using temperature-dependent force constants [28]. TEC calculated using temperature-dependent force constants is shown in the dash-dot green line in Fig. 2, which shows that this correction is small in the case of Al_2O_3 .

C. MLIP

We employ a MTP-based [39,40,57] MLIP to characterize the temperature-dependent potential surface of Al_2O_3 . The accuracy and effectiveness of this method have been demonstrated in previous studies [29,70]. A potential is trained for each temperature of this paper, i.e., at 500, 800, 1000, 1200, 1500, 1600, 1700, 1800, 1900, 2000, 2100, and 2200 K. The temperature interval is kept small at higher temperatures, as the focus of this paper is to study the flattening trend of κ at higher temperatures. The training database for each potential is prepared by AIMD with NVT ensemble for 500 steps with time step of 5 fs. The lattice structure for particular temperatures is expanded using TEC. A supercell of $3 \times 3 \times 3$ primitive cell containing 270 atoms is used in the simulation domain. Four independent AIMDs with randomly displaced initial atomic positions are performed at each temperature to better sample the potential energy surface. Energies, forces, and stresses are recorded together with corresponding atomic configurations to construct the training and testing database. The database is separated randomly maintaining 75% (1500 snapshots) for training and 25% (500 snapshots) for testing. The initial MTP of level 22 is selected to train the potential based on the accuracy and computational demand. The selected initial potential is trained for 1000 iteration steps with the minimum and maximum atomic interaction cutoffs of 1.2 and 5.5 Å, respectively.

D. GKMD

Once the MTP with a small error is developed, GKMD is performed by using the MLIP-LAMMPS package [39,58]. GKMD calculates the lattice thermal conductivity by integrating the heat current autocorrelation function based on the Green-Kubo formula [41,42]:

$$\kappa_{\text{GKMD}} = \frac{1}{3k_B T^2 V} \int_0^\infty \langle \vec{J}(0) \cdot \vec{J}(t) \rangle dt, \quad (1)$$

where k_B is the Boltzmann constant, V is volume of total simulation domain, T is temperature, $\vec{J}(t)$ is the heat current, and the angular bracket represents an autocorrelation. In LAMMPS, the heat current vector is calculated by the energy and forces of the system, which is obtained from the MTP.

In this paper, we employ a $7 \times 4 \times 3$ supercell of the conventional cell, containing 5042 atoms. The size effect is studied. Periodic boundary conditions are implemented in all three dimensions. The time step of GKMD is set to 1 fs. First, an NVT ensemble is run for 200 000 steps (0.2 ns) to fully stabilize the temperature of the system. Then an NVE ensemble is run for 200 000 steps (0.2 ns) to fully stabilize the system. Finally, another NVE ensemble is run for 800 000 steps with a correlation time of 200 ps, during which the heat current correlation is recorded. To mitigate the noise and intrinsic statistical error of GKMD, we conduct 16 independent runs with different initial velocities for each temperature. The ratio between the total running time and the correlation time is maintained >300 , which has been reported to be sufficient [71]. Since the temperatures in this paper are relatively high,

the difference between a classical statistics and a quantum statistics is neglected.

E. Temperature correction to force constants

The temperature-dependent harmonic and AFCs are extracted using the TDEP method [59,60] at 500, 1000, 1500, and 2000 K. The TDEP method extracts effective force constants at a certain temperature by fitting the potential energy of a series of atomic trajectory images at that temperature to the second, third, and fourth orders. Here, 1000 randomly displaced configurations are generated at each temperature to sample the potential surface. The forces, stress, and energies of these configurations are obtained from MTP at that temperature. The effect of the temperature is factored in by a thermal expansion, a temperature-dependent MTP trained from AIMD simulations at different temperatures, and a temperature-dependent displacement of atoms in the generated supercells.

F. Phonon and diffuson thermal conductivity by Wigner formalism

Using the force constants, the thermal conductivity is calculated by solving the Wigner's formalism [32,33]:

$$\kappa^{\alpha\beta} = \kappa_{\text{ph}}^{\alpha\beta} + \kappa_{\text{dif}}^{\alpha\beta}, \quad (2)$$

$$\kappa_{\text{ph}}^{\alpha\beta} = \frac{\hbar^2}{k_B T^2 V_c N_{\mathbf{q}}} \sum_{\mathbf{q}} \sum_j^{3n_b} v_{\mathbf{q},j}^\alpha v_{\mathbf{q},j}^\beta \omega_{\mathbf{q},j}^2 n_{\mathbf{q},j} (n_{\mathbf{q},j} + 1) \tau_{\mathbf{q},j}, \quad (3)$$

$$\kappa_{\text{dif}}^{\alpha\beta} = \frac{\hbar^2}{k_B T^2 V N_{\mathbf{q}}} \sum_{\mathbf{q}} \sum_{j \neq j'}^{3n, 3n} v_{\mathbf{q},j}^\alpha v_{\mathbf{q},j'}^\beta \frac{\omega_{\mathbf{q},j} + \omega_{\mathbf{q},j'}}{2} \frac{\omega_{\mathbf{q},j} n_{\mathbf{q},j} (n_{\mathbf{q},j} + 1) + \omega_{\mathbf{q},j'} n_{\mathbf{q},j'} (n_{\mathbf{q},j'} + 1)}{4(\omega_{\mathbf{q},j'} - \omega_{\mathbf{q},j})^2 + (\tau_{\mathbf{q},j}^{-1} + \tau_{\mathbf{q},j'}^{-1})^2} (\tau_{\mathbf{q},j}^{-1} + \tau_{\mathbf{q},j'}^{-1}), \quad (4)$$

$$\tau_{\mathbf{q},j}^{-1} = \tau_{3\text{ph}}^{-1} + \tau_{4\text{ph}}^{-1} + \tau_{\text{ph-iso}}^{-1}. \quad (5)$$

Here, α and β are cartesian directions; $\kappa_{\text{ph}}^{\alpha\beta}$ is the phonon particle thermal conductivity (or Peierls thermal conductivity); $\kappa_{\text{dif}}^{\alpha\beta}$ is the diffuson thermal conductivity; j and j' are phonon branches; ω is the angular frequency; v is the group velocity; and τ^{-1} is the phonon scattering rates, including 3ph, 4ph, and phonon-isotope scatterings. The convergence of ShengBTE at various \mathbf{q} -mesh densities is tested. Specifically, the 3ph calculation converges at a \mathbf{q} -mesh density of $18 \times 18 \times 18$, and the 3ph + 4ph calculation converges at $6 \times 6 \times 6$. The iterative solution to 3ph and phonon-isotope scattering is included, as implemented in ShengBTE. Here, 4ph scattering is taken at the relaxation time approximation level. The formalism of 3ph and 4ph scattering rates can be found in Ref. [27].

G. Radiation thermal conductivity

Like phonons, photons can also transport in materials. Analogous to phonon creation and annihilation (i.e., phonon scattering events), which limit the phonon mean free path (MFP), photon absorption and re-emission also limit the

photon MFP inside a material. When the size of a material is much larger than the phonon MFP, phonons transport diffusively, and the phonon thermal conductivity is approximately proportional to the phonon MFP. Similarly, when the size of a material is much larger than its photon MFP, the material is optically thick, and its radiation contribution to thermal conductivity is proportional to photon MFP. Based on the Rosseland model, the radiation contribution to thermal conductivity (κ_{rad}) of an optically thick material [18,72,73] is

$$\kappa_{\text{rad}} = \frac{16n^2(T)\sigma_{SB}T^3}{3\beta(T)}, \quad (6)$$

where $n(T)$ and $\beta(T)$ are the temperature-dependent refractive index and extinction coefficient, respectively; $\beta(T)$ gives the attenuation of the electromagnetic waves inside the material and is the inverse of photon MFP; and $n(T)$ and $\beta(T)$ are given by

$$n(T) = \int_0^\infty n(\lambda, T) \frac{\partial E_{b\lambda}}{\partial E_b} d\lambda, \quad (7)$$

$$\frac{1}{\beta(T)} = \int_0^\infty \frac{1}{\alpha(\lambda, T)} \frac{\partial E_{b\lambda}}{\partial E_b} d\lambda. \quad (8)$$

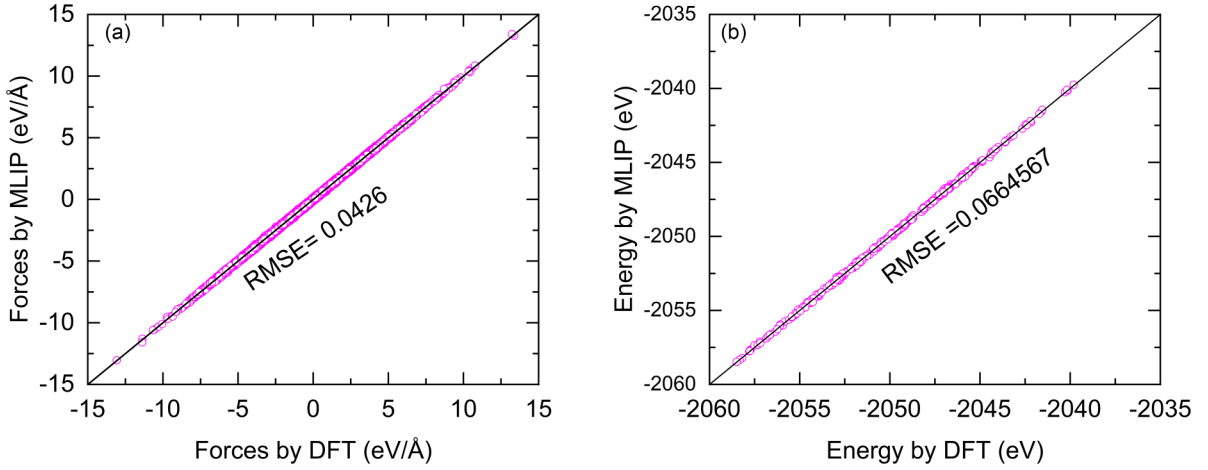


FIG. 3. Comparison of (a) forces and (b) energies obtained from machine-learned interatomic potential with density functional theory (DFT) calculations.

Here, σ_{SB} is the Stefan-Boltzmann constant. The spectral refractive index $n(\lambda, T)$ and spectral absorption coefficient $\alpha(\lambda, T)$ can be calculated from the dielectric function $\epsilon(\lambda, T)$ as

$$n^2(\lambda, T) = \frac{1}{2} [|\epsilon(\omega, T)| + \epsilon_{re}(\omega, T)], \quad (9)$$

$$\alpha(\lambda, T) = \frac{4\pi k}{\lambda} = \frac{2\sqrt{2}\pi}{\lambda} [|\epsilon(\omega, T)| - \epsilon_{re}(\omega, T)]^{1/2}, \quad (10)$$

where ϵ_{re} is the real part of ϵ , and $k(\lambda, T)$ is the spectral extinction coefficient given by

$$k(\lambda, T) = \frac{1}{\sqrt{2}} [|\epsilon(\omega, T)| - \epsilon_{re}(\omega, T)]^{1/2}. \quad (11)$$

The dielectric function $\epsilon(\omega, T)$ can be predicted using the four-parameter Lorentz oscillator model [47,48] as

$$\epsilon(\omega, T) = \epsilon(\infty) \prod_j \frac{\omega_{j,LO}^2 - \omega^2 + i\Gamma_{j,LO}\omega}{\omega_{j,TO}^2 - \omega^2 + i\Gamma_{j,TO}\omega}, \quad (12)$$

where Γ is the same as the phonon scattering rate, i.e., $\Gamma = \tau^{-1}$; ω is the phonon or photon angular frequency, i.e., $\omega = 2\pi f$; j runs through all the infrared active transverse optical (TO) and longitudinal optical (LO) branches; i is the imaginary unit number; and $\epsilon(\infty)$ is the dielectric function at the high-frequency limit which is calculated from the density functional perturbation theory [74]. The calculated values are 3.21 and 3.23 for ordinary and extraordinary rays, which match well with the experimental values of 3.2 and 3.1 [75]. The details of the calculation of $\epsilon(\omega, T)$ are like that of Ref. [76].

III. RESULTS

A. MLIP and GKMD

The MTP is trained by using the stress, forces, and energies obtained from AIMD calculations. The training and testing errors are $<5\%$ for each potential trained at various temperatures. To further verify the accuracy of the trained potentials, we extracted the forces and energies of the test dataset using the MTP. Note that this test dataset is not used

to train the potential and is selected randomly. The extracted forces and energy from the MTP are plotted against the forces and energies obtained from DFT calculations. As seen in Fig. 3, all the points lie along the diagonal with low root mean square error of 0.0426 eV/Å and 0.0664 eV for forces and energies, respectively. This shows that the MTP could accurately reproduce the forces and energies of the configurations and represent the actual potential surface with accuracy comparable with DFT calculation.

Using the MTP, GKMD is conducted to calculate the lattice thermal conductivity (κ_{GKMD}), as shown in Fig. 4. The average thermal conductivity is obtained by integrating the autocorrelated heat flux with correlation time. As seen in the inset of Fig. 4, the average thermal conductivity converges, suggesting that the parameters used in our calculations are appropriate. The κ_{GKMD} shows a flattening and slight increasing trend at ultrahigh temperatures, which agrees reasonably well with experimental data. This further demonstrates the

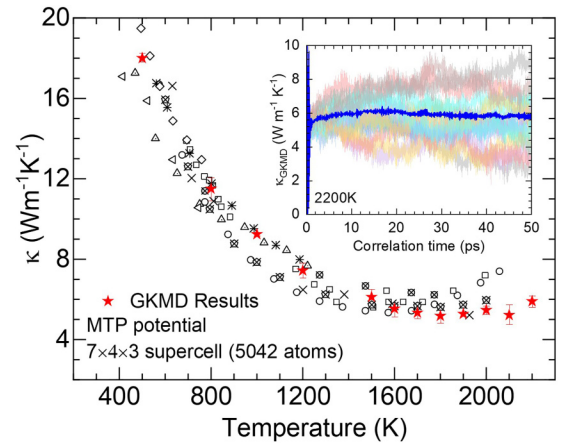


FIG. 4. Thermal conductivity of Al_2O_3 at various temperatures obtained by Green-Kubo molecular dynamics (GKMD) using machine-learning interatomic potentials (MLIPs). The experimental data (open dots) [16–25] are shown for comparison. Inset shows several independent runs and their average as a function of correlation time for 2200 K.

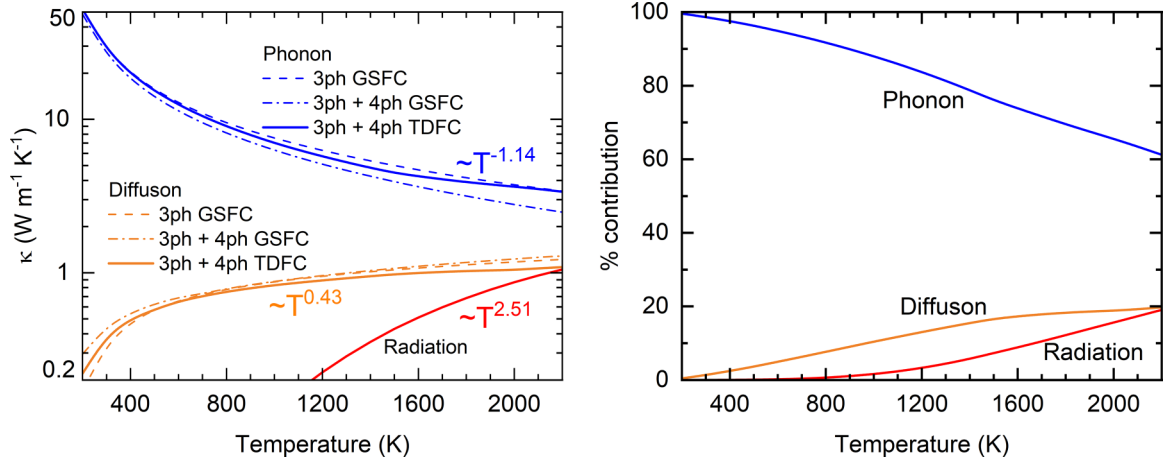


FIG. 5. (a) Phonon, diffuson, and radiation thermal conductivities in Al_2O_3 as a function of temperature. The power laws are fitted using the calculated data. (b) The relative contributions from phonon, diffuson, and radiation.

high accuracy of the trained MTP. However, the experimental data show much increasing thermal conductivity at ultrahigh temperatures, which could not be captured by the GKMD.

B. Phonon, diffuson, and radiation thermal conductivity

In the following, we track the changes of κ at low temperature (300 K), high temperature (1200 K), and ultrahigh temperature (2200 K) when we gradually increase the calculation comprehensivity and include the contributions of phonon (κ_{ph}), diffuson (κ_{dif}), and radiation (κ_{rad}). First, we calculate the basic 3ph thermal conductivity using ground-state force constants (GSFCs), shown in the blue-dashed line in Fig. 5(a), which follows $\kappa \sim T^{-1}$ law. The κ_{ph} is 28.59, 6.26, and $3.4 \text{ W m}^{-1} \text{ K}^{-1}$ at 300, 1200, and 2200 K, respectively.

The 3ph rates at 300 and 2000 K are shown in Fig. 6(a), which increases with temperature. Second, we include the 4ph scattering using GSFC, shown in dash-dotted blue line, which decreases κ_{ph} by 8, 18, and 24% to 26.30, 5.09, and $2.48 \text{ W m}^{-1} \text{ K}^{-1}$ at the three temperatures, respectively. The effect of 4ph rates is not that strong. It is primarily due to the fact that the crowd phonon branches [Fig. 6(b)] in Al_2O_3 allow the energy and momentum selection rules of 3ph scattering to be easily satisfied. With strong 3ph scattering, the relative importance of 4ph scattering is naturally small. Third, we replace the GSFC by the temperature-dependent force constant (TDFC), which is found to increase κ_{ph} by 8, 13, and 36% to 28.43, 5.73, and $3.37 \text{ W m}^{-1} \text{ K}^{-1}$ at the three temperatures, respectively. This increase is due to the combined effect of temperature correction to the lattice constant and interatomic

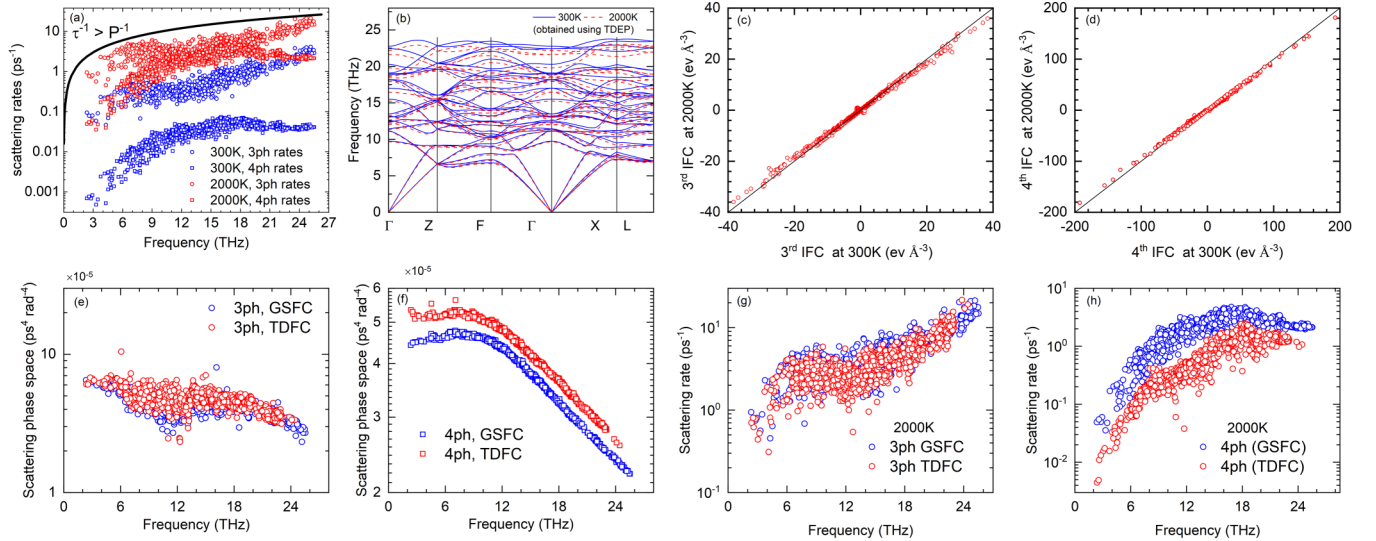


FIG. 6. (a) Three-phonon (3ph) and four-phonon (4ph) scattering rates at 300 and 2000 K, respectively. The black line serves as a guideline for the comparison of phonon lifetime with its period. (b) Temperature dependence of phonon dispersion [calculated at 300 and 2000 K using the force constant obtained from temperature-dependent effective potential (TDEP)]. (c) and (d) The temperature softening of third and fourth orders of interatomic force constants (IFCs). (e) and (f) Comparison of scattering phase space using ground state force constants and temperature-dependent force constants for 3ph and 4ph. (g) and (h) Decrease in 3ph rates and 4ph rates at 2000 K due to temperature correction to force constants.

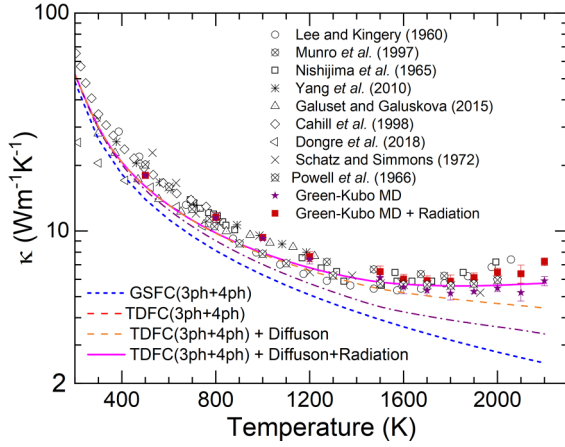


FIG. 7. The variation of thermal conductivity prediction of Al_2O_3 using various approaches. Experimental thermal conductivity data from Refs. [16–25] are also shown for comparison.

force constants. At elevated temperatures, phonon dispersion gets softened due to lattice expansion and harmonic force constant softening [Fig. 6(b)]. This results in an increase in 3ph and 4ph scattering phase space, as shown in Figs. 6(e) and 6(f), due to the change in the energy and momentum conservation selection rule. At the same time, finite-temperature AFC softening decreases the scattering cross-section, as shown in Figs. 6(c) and 6(d), which results in the decrease in 3ph and 4ph rates, as shown in Figs. 6(g) and 6(h). In fact, TD 2FC tends to increase the scattering rates by increasing the scattering phase space. It is due to the more pronounced reduction in TD 3FC and TD 4FC that leads to the decrease in scattering rates. Overall, incorporating TDFC increases κ_{ph} and flattens κ_{ph} curve at high temperatures.

One interesting phenomenon seen in Fig. 5(a) is that κ_{ph} using GSFC and 3ph rates (dashed blue line) and κ_{ph} using TDFC and 3ph + 4ph rates (solid-blue line) agree with each other with reasonable accuracy at high temperatures. This is due to the competing effect of 4ph scattering and TDFC in thermal conductivity, considering 4ph rates decrease κ_{ph} while TDFC increases it. In the case of Al_2O_3 , these two opposite effects are found to cancel each other. This also introduces the possibility of an error-cancellation effect on other complex materials, where the effect of TDFC and 4ph rates cancel each other, and κ_{ph} computed using GSFC and 3ph scattering matches with experimental data.

The diffuson thermal conductivity (κ_{dif}) increases with temperature at low and intermediate temperatures and becomes flat at ultrahigh temperatures, as shown in Fig. 5(a). Using GSFC, κ_{dif} is $\sim 0.44 \text{ W m}^{-1} \text{ K}^{-1}$ at 300 K which increases to 0.95 and $1.28 \text{ W m}^{-1} \text{ K}^{-1}$ at 1200 and 2200 K, respectively. At high temperatures, the phonon linewidth increases, which increases the phonon tunneling probability and increases κ_{dif} . Using TDFC, κ_{dif} decreases by 13, 7, and 16% to 0.38, 0.89, and 1.08 at 300, 1200, and 2200 K, respectively. Adding κ_{dif} to κ_{ph} makes κ flatter at high temperatures, as shown in the dashed orange line in Fig. 7. Here, $\kappa_{\text{ph}} + \kappa_{\text{dif}}$ matches experimental data at intermediate to high temperatures but could not explain the increase in thermal conductivity at ultrahigh temperatures.

Also, $\kappa_{\text{ph}} + \kappa_{\text{dif}}$ obtained from the Wigner formalism matches the GKMD results throughout the temperatures. This alignment underscores the capability of both GKMD and the Wigner formalism to effectively capture κ_{ph} and κ_{dif} . Further, the good agreement between these two different approaches supports the Wigner formalism as well as the accuracy and consistency of our calculations.

The radiation thermal conductivity (κ_{rad}) is negligibly small at room temperature, but it increases with temperature and reaches 0.22 and $1.05 \text{ W m}^{-1} \text{ K}^{-1}$ at 1200 and 2200 K, respectively. The partial contributions of κ_{ph} , κ_{dif} , and κ_{rad} are shown in Fig. 5(b). As seen, κ_{ph} decays with temperature, κ_{dif} increases and saturates with temperature, while κ_{rad} increases rapidly with temperature. At room temperature, κ_{dif} and κ_{rad} are almost negligible, resulting in $\kappa \approx \kappa_{\text{ph}}$ i.e., κ_{ph} contributes to almost 100% of κ . At a high temperature of 1200 K, κ_{dif} increases significantly and contributes 13%, and the κ_{rad} contribution is 3.27%. At an ultrahigh temperature of 2200 K, κ_{rad} becomes significant as well. At this temperature, κ_{ph} , κ_{dif} , and κ_{rad} contribute 61.2, 19.7, and 19.1%, respectively.

When κ_{ph} , κ_{dif} , and κ_{rad} are summed up together, κ reaches 28.81, 6.85, and $5.51 \text{ W m}^{-1} \text{ K}^{-1}$ at 300, 1200, and 2200 K, respectively. This is shown in the solid-magenta line in Fig. 7, which matches well with the experimental data. This shows that the total thermal transport comes from the contribution of κ_{ph} , κ_{dif} , and κ_{rad} . The red points in the graph show κ obtained by summing up κ_{GKMD} and κ_{rad} , which also matches with experimental data.

The scaling laws of κ_{ph} , κ_{dif} , and κ_{rad} with respect to temperature are shown in Fig. 5. For Al_2O_3 , we find that κ_{ph} decays approximately as $\sim T^{-1.14}$ after considering 4ph scattering as well as finite-temperature corrections to the lattice constant, harmonic, and AFCs. This is slightly different from $\kappa_{\text{ph}} \sim T^{-1.19}$ obtained from using ground-state force constants. Here, κ_{dif} increases roughly as $\sim T^{0.43}$. Also, κ_{rad} increases as $\sim T^{2.51}$, being slightly smaller than $\sim T^3$ due to the increase of phonon linewidth with temperature, which increases the photon extinction coefficient and reduces the photon MFP. These scaling laws are of interest when interpreting or predicting the thermal conductivity trends of other materials as well. Details of power-law fittings can be found in the Supplemental Material [77].

IV. DISCUSSION

A. Phonon lifetime and MFP

Based on the diffuson theory, the phonons are characterized as either normal phonons or diffusonlike phonons based on Ioffe-Regel limit criteria [78,79]. The first criterion compares the lifetime (τ) of phonons with their period (P), stating that phonon modes with their τ smaller than P cannot be treated as particles anymore and should be treated as diffusons. In this condition, phonon modes exhibit wavelike nature, which allows them to tunnel between close eigenstates and transport heat diffusively. Figure 6(a) shows the 3ph and 4ph rates, along with P^{-1} (shown in the black-solid line). As seen, both 3ph and 4ph rates, even at the higher temperature of 2000 K, are smaller than P^{-1} (equivalently $\tau > P$), showing that all the phonon modes are normal phonons. Similarly, the second criterion states that phonon modes with MFP smaller

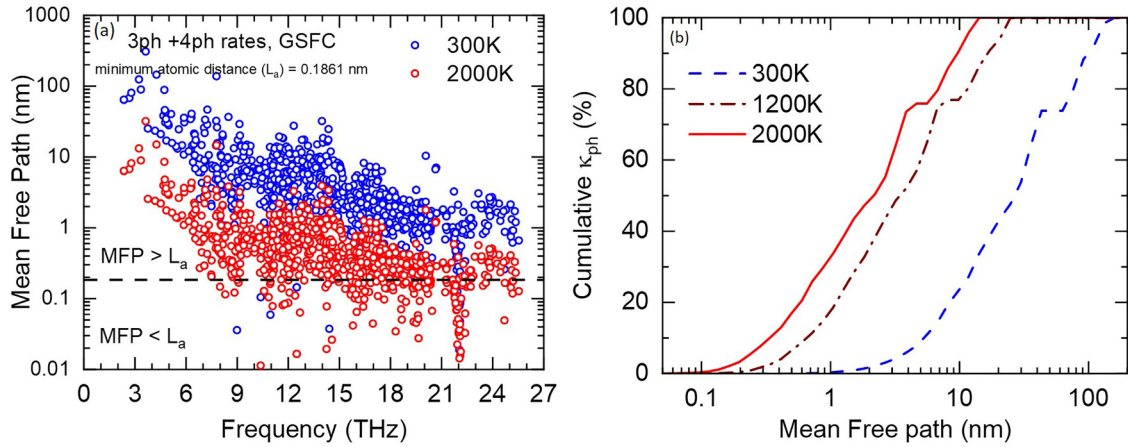


FIG. 8. (a) Mean free path (MFP) of the phonon modes compared with minimum atomic spacing (b) cumulative phonon thermal conductivity as a function of phonon MFP.

than the minimum interatomic distance (L_a) become diffuson or diffusonlike phonons. As seen in Fig. 8(a), some phonon modes in the optical region (with frequency > 6 THz) have $MFP < L_a$ at 300 K and are diffusonlike phonons. The number of diffusonlike phonons increases with temperature, and nearly one-third of the optical phonons becomes diffusonlike phonons at 2000 K. This explains the increase in diffuson thermal conductivity with temperature as more phonon modes become diffusonlike phonons at higher temperatures. Note that, in the Wigner formalism, all phonons are both particles and diffusons simultaneously at all temperatures. All phonons contribute to heat conduction through dual channels—particle and diffuson. As temperature increases, the diffuson nature of more phonons weighs more than their particle nature.

Figure 8(b) shows the cumulative κ_{ph} with respect to MFP. At 300K, 80% of κ_{ph} comes from phonons with $MFP < 50$ nm. This value decreases to 5 nm as the temperature increases to 2000 K. As the experimental samples have grain size on the order of microns, κ reported in experimental studies are not suffered by grain boundary scattering.

B. Radiation heat transfer

To investigate the reason behind the radiation heat transfer, we calculate the spectral radiative properties of Al_2O_3 using the Lorentz oscillator model, which uses the frequency and damping of infrared (IR) active phonon modes at the Γ point. Based on symmetry analysis [80–82], the phonon modes on

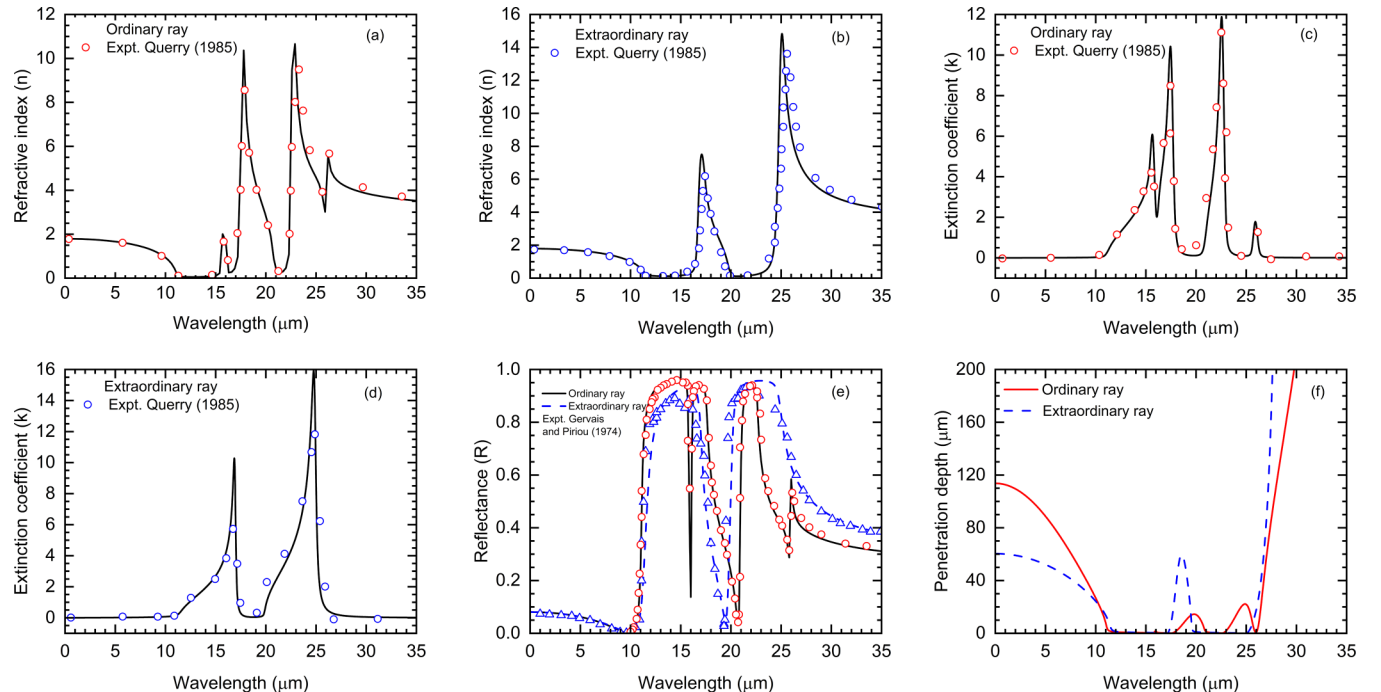


FIG. 9. Radiative thermal properties of Al_2O_3 at room temperature calculated in this paper from first principles (curves) compared with experimental data (symbols). (a) and (b) Refractive index. (c) and (d) Extinction coefficient. (e) Reflectance. (f) Photon penetration depth.

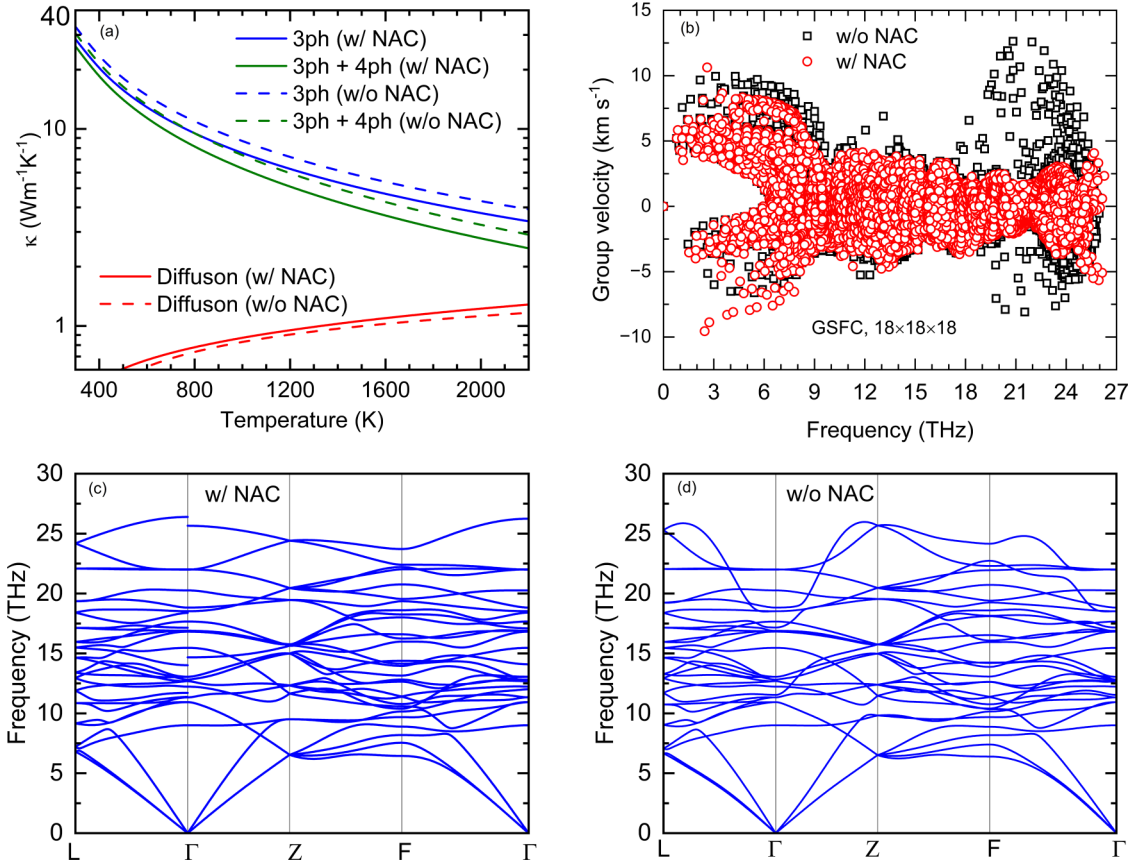


FIG. 10. Effect of nonanalytical correction (NAC) on (a) phonon thermal conductivity, (b) group velocities of phonon, and (c) and (d) phonon band dispersion.

Al₂O₃ are $2A_{1g} + 2A_{1u} + 3A_{2g} + 2A_{2u} + 4E_u + 5E_g$. Among these modes, the A_{2u} (extraordinary ray with the electric field vector parallel to the z axis) and E_u (ordinary ray with the electric field vector perpendicular to the z axis) species are IR-active modes, A_{1g} and E_g are Raman active modes, and A_{2g} and A_{1u} are spectroscopically inactive. The details on determining TO and LO branch indexes of IR active modes are discussed in Ref. [76,83].

The radiative properties evaluated at room temperature are shown in Fig. 9. The spectral refractive index (n) and extinction coefficient (k) are shown in Figs. 9(a)–9(d), respectively. The experimental data from Query [84] are also shown for comparison, which shows a close agreement. The reflectance is calculated from the dielectric function or refractive index as

$$R = \left| \frac{\sqrt{\epsilon} - 1}{\sqrt{\epsilon} + 1} \right|^2 = \frac{(1 - n)^2 + k^2}{(1 + n)^2 + k^2}. \quad (13)$$

The spectral reflectance is shown in Fig. 9(e), which matches well with the experimental data [48,75].

The extinction coefficient measures the attenuation of radiative waves inside the medium and is inversely correlated to the photon MFP. It depends on the imaginary part of the dielectric function and is sensitive to the damping factor or phonon linewidth. Thus, the temperature-dependent phonon linewidth is used to accurately calculate the extinction coefficient at higher temperatures. Note that the value for the extinction coefficient varies with the size of the material and

was reported from 0.02 for bulk material [84] to 0.00008 for the thin film of 500 nm [85] at 1 μ m wavelength. This results in significantly different κ_{rad} on bulk materials and thin film. The present calculation is based on the bulk material and is compared with the experimental data reported for bulk material by Query [84]. From the spectral extinction coefficient, we can see that Al₂O₃ is nearly transparent in the near-IR range, with a penetration depth of ~ 110 μ m for ordinary rays and ~ 60 μ m for extraordinary rays in this range [Fig. 9(f)]. In the case of thin film, the photon might pass through the material instead of interacting with it.

The present calculation is based on the Rosseland model, which assumes the materials to be optically thick, where the photon gets absorbed in the medium and re-emitted and reabsorbed. In this scenario, the medium behaves as a participating medium and leads to the radiation thermal transport, as discussed in the previous papers [18,21,24,43–46]. The dominant radiation in the high-temperature region lies in the near-IR range, as per Wein's law ($\lambda_{\text{dom}}T = 2898$ μ m K), for which the penetration depth is on the order of ~ 100 μ m. Since the experimental sample are in millimeters or higher [18,19,75,84], the optically thick medium approximation used in our calculations is justified.

C. Effect of nonanalytical correction

As shown in Fig. 10(a), the consideration of the nonanalytical correction (NAC) decreases κ_{ph} moderately and increases

κ_{dif} slightly. The comparison is made for the calculation made with the ground-state force constant. The NAC consideration decreases κ_{ph} from 30.58, 5.95, and 2.90 $\text{W m}^{-1} \text{K}^{-1}$ to 26.30, 5.09, and 2.48 $\text{W m}^{-1} \text{K}^{-1}$ at the temperatures of 300, 1200, and 2200 K, respectively. Whereas κ_{dif} changes from 0.48, 0.90, and 1.24 $\text{W m}^{-1} \text{K}^{-1}$ to 0.44, 0.95, and 1.28 $\text{W m}^{-1} \text{K}^{-1}$, respectively. Overall, κ is overestimated if the NAC is not considered. This overestimation is due to the higher group velocities without the NAC [Fig. 10(b)]. The phonon scattering rates are not affected significantly. The change of group velocities is understandable since the NAC causes TO-LO branch splitting, which flattens some branches in phonon dispersion, as shown in Figs. 10(c) and 10(d), and then reduces the group velocities.

V. CONCLUSIONS

In conclusion, in this paper, we present the accurate first-principles prediction of the thermal conductivity of Al_2O_3 from room temperature to near the melting point (2200 K). The lattice thermal conductivity is found to be composed of contributions of phonon, diffuson, and radiation. The following conclusions are drawn. (1) Including all-temperature effects on phonon, diffuson, and radiation can reproduce the flattening and increasing trend of lattice thermal conductivity at high to ultrahigh temperatures. (2) Phonon particle thermal conductivity decays approximately as $\sim T^{-1.14}$. Diffuson thermal conductivity increases roughly as $\sim T^{0.43}$. Radiation thermal conductivity increases as $\sim T^{2.51}$. (3) At room temperature, phonon, diffuson, and radiation contribute 98.7, 1.3, and 0%, respectively. (4) At 2200 K, they contribute 61.2, 19.7, and 19.1%, respectively. (5) 4ph scattering is important at ultrahigh temperature, decreasing the phonon thermal conductivity by a maximum of 24%. (6) The finite-temperature softening effects of harmonic and AFCs can increase the

phonon thermal conductivity by a maximum of 36% at ultrahigh temperatures. (7) The thermal conductivity from GKMD agrees reasonably well with the Wigner formalism, indicating that GKMD captures both the particle and wave nature of phonons. (8) The dominant phonon MFP of Al_2O_3 is 50 and 5 nm at 300 and 2200 K, respectively, indicating that it does not suffer from size effects for most experimental samples. (9) The photon penetration depth is ~ 100 nm, indicating that the ballistic effect of photon transport needs to be considered in the measurement of thermal conductivity of Al_2O_3 thin films when the film thickness is on the order of 100 nm at high temperatures. We hope our findings have deepened the understanding of lattice thermal conductivity at ultrahigh temperatures for complex crystals and will lead to more materials exploration for ultrahigh temperature applications.

Source data are provided along with this paper. All other data that support the plots within this paper and the codes used in this paper are available from the corresponding authors on reasonable request.

ACKNOWLEDGMENTS

This paper is supported by the National Science Foundation (NSF) (Award No. CBET 2212830). The simulations used Bridges-2 at Pittsburgh Supercomputing Center through allocation PHY220002 from the Advanced Cyberinfrastructure Coordination Ecosystem: Services & Support program, which is supported by NSF Grants No. 2138259, No. 2138286, No. 2138307, No. 2137603, and No. 2138296. The support and resources from the Center for High Performance Computing at the University of Utah are gratefully acknowledged.

T.F. conceived the idea and guided the project. J.T. performed the simulations and wrote the original manuscript. J.T. and T.F. both revised the manuscript.

The authors declare no competing interests.

-
- [1] D. R. Clarke and S. R. Phillpot, Thermal barrier coating materials, *Mater. Today* **8**, 22 (2005).
- [2] B. Liu, Y. Liu, C. Zhu, H. Xiang, H. Chen, L. Sun, Y. Gao, and Y. Zhou, Advances on strategies for searching for next generation thermal barrier coating materials, *J. Mater. Sci. Technol.* **35**, 833 (2019).
- [3] J. Chen, K. Chen, Y. G. Liu, Z. H. Huang, M. H. Fang, and J. T. Huang, Effect of Al_2O_3 addition on properties of non-sintered SiC-Si₃N₄ composite refractory materials, *Int. J. Refract. Met. Hard Mater.* **46**, 6 (2014).
- [4] C. Atzenhofer, S. Gschiel, and H. Harmuth, Phase formation in Al_2O_3 -C refractories with Al addition, *J. Eur. Ceram. Soc.* **37**, 1805 (2017).
- [5] Y. Meng, G. Gong, D. Wei, and Y. Xie, In situ high temperature x-ray diffraction study on high strength aluminous porcelain insulator with the Al_2O_3 -SiO₂-K₂O-Na₂O system, *Appl. Clay Sci.* **132**, 760 (2016).
- [6] Y. Liu, H. Jiang, X. Zhao, X. Deng, and W. Zhang, High temperature electrical insulation and adhesion of nanocrystalline YSZ/ Al_2O_3 composite film for thin-film thermocouples on ni-based superalloy substrates, *Appl. Surf. Sci.* **579**, 152169 (2022).
- [7] R. A. Guyer, Phonon gas: A lattice Boltzmann description, *Phys. Rev. E* **50**, 4596 (1994).
- [8] W. Lv and A. Henry, Examining the validity of the phonon gas model in amorphous materials, *Sci. Rep.* **6**, 37675 (2016).
- [9] T. Sun and P. B. Allen, Lattice thermal conductivity: Computations and theory of the high-temperature breakdown of the phonon-gas model, *Phys. Rev. B* **82**, 224305 (2010).
- [10] W. H. Tuan, R. Z. Chen, T. C. Wang, C. H. Cheng, and P. S. Kuo, Mechanical properties of $\text{Al}_2\text{O}_3/\text{ZrO}_2$ composites, *J. Eur. Ceram. Soc.* **22**, 2827 (2002).
- [11] M. Kok, Production and mechanical properties of Al_2O_3 particle-reinforced 2024 aluminium alloy composites, *J. Mater. Process. Technol.* **161**, 381 (2005).
- [12] Y. H. Fei, C. Z. Huang, H. L. Liu, and B. Zou, Mechanical properties of Al_2O_3 -TiC-TiN ceramic tool materials, *Ceram. Int.* **40**, 10205 (2014).

- [13] R. H. French, Electronic band structure of Al_2O_3 , with comparison to Alon and AlN, *J. Am. Ceram. Soc.* **73**, 477 (1990).
- [14] K. Z. Rajab, M. Naftaly, E. H. Linfield, J. C. Nino, D. Arenas, D. Tanner, R. Mitra, and M. Lanagan, Broadband dielectric characterization of aluminum oxide (Al_2O_3), *J. Microelectron. Electron. Packag.* **5**, 2 (2008).
- [15] S. J. Schneider and C. L. McDaniel, Effect of environment upon the melting point of Al_2O_3 , *J. Res. NBS A Phys. Chem.* **71**, 317 (1967).
- [16] D. G. Cahill, S.-M. Lee, and T. I. Selinder, Thermal conductivity of κ - Al_2O_3 and α - Al_2O_3 wear-resistant coatings, *J. Appl. Phys.* **83**, 5783 (1998).
- [17] R. G. Munro, Evaluated material properties for a sintered α -alumina, *J. Am. Ceram. Soc.* **80**, 1919 (1997).
- [18] D. W. Lee and W. D. Kingery, Radiation energy transfer and thermal conductivity of ceramic oxides, *J. Am. Ceram. Soc.* **43**, 594 (1960).
- [19] T. Nishijima, T. Kawada, and A. Ishihata, Thermal conductivity of sintered UO, and Al_2O_3 at high temperatures, *J. Am. Ceram. Soc.* **48**, 31 (1965).
- [20] F. Yang, X. Zhao, and P. Xiao, Thermal conductivities of YSZ/ Al_2O_3 composites, *J. Eur. Ceram. Soc.* **30**, 3111 (2010).
- [21] J. F. Schatz and G. Simmons, Thermal conductivity of earth materials at high temperatures, *J. Geophys. Res.* **77**, 6966 (1972).
- [22] M. Parchovianský, D. Galusek, P. Švančárek, J. Sedláček, and P. Šajgalík, Thermal behavior, electrical conductivity and microstructure of hot pressed $\text{Al}_2\text{O}_3/\text{SiC}$ nanocomposites, *Ceram. Int.* **40**, 14421 (2014).
- [23] R. W. Powell, C. Y. Ho, and P. E. Liley, *Thermal Conductivity of Selected Materials* (US Department of Commerce, National Bureau of Standards, Washington, DC, 1966), Vol. 8.
- [24] M. McQuarrie, Thermal conductivity: VII, analysis of variation of conductivity with temperature for Al_2O_3 , BeO, and MgO, *J. Am. Ceram. Soc.* **37**, 91 (1954).
- [25] D. S. Smith, S. Fayette, S. Grandjean, C. Martin, R. Telle, and T. Tonnesen, Thermal resistance of grain boundaries in alumina ceramics and refractories, *J. Am. Ceram. Soc.* **86**, 105 (2003).
- [26] T. Feng, L. Lindsay, and X. Ruan, Four-phonon scattering significantly reduces intrinsic thermal conductivity of solids, *Phys. Rev. B* **96**, 161201(R) (2017).
- [27] T. Feng and X. Ruan, Quantum mechanical prediction of four-phonon scattering rates and reduced thermal conductivity of solids, *Phys. Rev. B* **93**, 045202 (2016).
- [28] J. Tiwari and T. Feng, Intrinsic thermal conductivity of ZrC from low to ultrahigh temperatures: A critical revisit, *Phys. Rev. Mater.* **7**, 065001 (2023).
- [29] X. Yang, J. Tiwari, and T. Feng, Reduced anharmonic phonon scattering cross-section slows the decrease of thermal conductivity with temperature, *Mater. Today Phys.* **24**, 100689 (2022).
- [30] R. J. Hardy, Energy-flux operator for a lattice, *Phys. Rev.* **132**, 168 (1963).
- [31] P. B. Allen and J. L. Feldman, Thermal conductivity of glasses: Theory and application to amorphous Si, *Phys. Rev. Lett.* **62**, 645 (1989).
- [32] M. Simoncelli, N. Marzari, and F. Mauri, Wigner formulation of thermal transport in solids, *Phys. Rev. X* **12**, 041011 (2022).
- [33] M. Simoncelli, N. Marzari, and F. Mauri, Unified theory of thermal transport in crystals and glasses, *Nat. Phys.* **15**, 809 (2019).
- [34] R. Hanus, J. George, M. Wood, A. Bonkowski, Y. Cheng, D. L. Abernathy, M. E. Manley, G. Hautier, G. J. Snyder, and R. P. Hermann, Uncovering design principles for amorphous-like heat conduction using two-channel lattice dynamics, *Mater. Today Phys.* **18**, 100344 (2021).
- [35] T. Pandey, M. H. Du, D. S. Parker, and L. Lindsay, Origin of ultralow phonon transport and strong anharmonicity in lead-free halide perovskites, *Mater. Today Phys.* **28**, 100881 (2022).
- [36] Z. Zeng, C. Zhang, N. Ouyang, and Y. Chen, Extreme in-plane phonon blocking in simple chainlike crystals, *Phys. Rev. B* **106**, 054302 (2022).
- [37] Y. Xia, V. Ozoliņš, and C. Wolverton, Microscopic mechanisms of glasslike lattice thermal transport in cubic $\text{Cu}_{12}\text{Sb}_4\text{S}_{13}$ tetrahedrites, *Phys. Rev. Lett.* **125**, 085901 (2020).
- [38] A. V. Shapeev, Moment tensor potentials: A class of systematically improvable interatomic potentials, *Multiscale Model. Simul.* **14**, 1153 (2016).
- [39] I. S. Novikov, K. Gubaev, E. V. Podryabinkin, and A. V. Shapeev, The MLIP package: Moment tensor potentials with MPI and active learning, *Mach. Learn. Sci. Technol.* **2**, 025002 (2021).
- [40] E. V. Podryabinkin and A. V. Shapeev, Active learning of linearly parametrized interatomic potentials, *Comput. Mater. Sci.* **140**, 171 (2017).
- [41] M. S. Green, Markoff random processes and the statistical mechanics of time-dependent phenomena. II. Irreversible processes in fluids, *J. Chem. Phys.* **22**, 398 (1954).
- [42] R. Kubo, Statistical-mechanical theory of irreversible processes. I. General theory and simple applications to magnetic and conduction problems, *J. Phys. Soc. Jpn.* **12**, 570 (1957).
- [43] F. R. Charvat and W. D. Kingery, Thermal conductivity: XIII, effect of microstructure on conductivity of single-phase ceramics, *J. Am. Ceram. Soc.* **40**, 306 (1957).
- [44] B. S. Kellett, Transmission of radiation through glass in tank furnaces, *J. Soc. Glas. Tech* **36**, 115 (1952).
- [45] W. D. Kingery, Thermal conductivity: XII, temperature dependence of conductivity for single-phase ceramics, *J. Am. Ceram. Soc.* **38**, 251 (1955).
- [46] B. S. Kellett, The steady flow of heat through hot glass, *JOSA* **42**, 339 (1952).
- [47] A. S. Barker, Jr., Transverse and longitudinal optic mode study in MgF_2 and ZnF_2 , *Phys. Rev.* **136**, A1290 (1964).
- [48] F. Gervais and B. Piriou, Anharmonicity in several-polar-mode crystals: Adjusting phonon self-energy of LO and to Modes in Al_2O_3 and TiO_2 to fit infrared reflectivity, *J. Phys. C: Solid State Phys.* **7**, 2374 (1974).
- [49] G. Kresse and J. Hafner, *Ab initio* molecular dynamics for liquid metals, *Phys. Rev. B* **47**, 558 (1993).
- [50] G. Kresse and J. Furthmüller, Efficiency of *ab-initio* total energy calculations for metals and semiconductors using a plane-wave basis set, *Comput. Mater. Sci.* **6**, 15 (1996).
- [51] J. P. Perdew, K. Burke, and M. Ernzerhof, Generalized gradient approximation made simple, *Phys. Rev. Lett.* **77**, 3865 (1996).
- [52] J. P. Perdew, A. Ruzsinszky, G. I. Csonka, O. A. Vydrov, G. E. Scuseria, L. A. Constantin, X. Zhou, and K. Burke, Restoring the density-gradient expansion for exchange in solids and surfaces, *Phys. Rev. Lett.* **100**, 136406 (2008).
- [53] J. Breeze, *Temperature and Frequency Dependence of Complex Permittivity in Metal Oxide Dielectrics: Theory, Modelling and Measurement* (Springer, Cham, 2016).

- [54] W. E. Lee and K. P. D. Lagerlof, Structural and electron diffraction data for sapphire (α - Al_2O_3), *J. Electron. Microsc. Tech.* **2**, 247 (1985).
- [55] A. Togo and I. Tanaka, First principles phonon calculations in materials science, *Scr. Mater.* **108**, 1 (2015).
- [56] W. W. Li, J. Carrete, N. A. N. A. Katcho, and N. Mingo, ShengBTE: A solver of the Boltzmann transport equation for phonons, *Comput. Phys. Commun.* **185**, 1747 (2014).
- [57] K. Gubaev, E. V. Podryabinkin, and A. V. Shapeev, Machine learning of molecular properties: Locality and active learning, *J. Chem. Phys.* **148**, 241722 (2018).
- [58] S. Plimpton, Fast parallel algorithms for short-range molecular dynamics, *J. Comput. Phys.* **117**, 1 (1995).
- [59] O. Hellman and I. A. Abrikosov, Temperature-dependent effective third-order interatomic force constants from first principles, *Phys. Rev. B* **88**, 144301 (2013).
- [60] O. Hellman, P. Steneteg, I. A. Abrikosov, and S. I. Simak, Temperature dependent effective potential method for accurate free energy calculations of solids, *Phys. Rev. B* **87**, 104111 (2013).
- [61] T. Feng, X. Yang, and X. Ruan, Phonon anharmonic frequency shift induced by four-phonon scattering calculated from first principles, *J. Appl. Phys.* **124**, 145101 (2018).
- [62] N. Soga and O. L. Anderson, High-temperature elastic properties of polycrystalline MgO and Al_2O_3 , *J. Am. Ceram. Soc.* **49**, 355 (1966).
- [63] T. Tohei, Y. Watanabe, H. S. Lee, and Y. Ikuhara, First principles calculation of thermal expansion coefficients of pure and Cr doped α -alumina crystals, *J. Appl. Phys.* **120**, 142106 (2016).
- [64] Y. S. Touloukian, R. K. Kirby, E. R. Taylor, and T. Y. R. Lee, *Thermophysical Properties of Matter—The TPRC Data Series. Volume 13. Thermal Expansion—Nonmetallic Solids* (IFI/Plenum, New York, 1977).
- [65] C. J. Engberg and E. H. Zehms, Thermal expansion of Al_2O_3 , BeO, MgO, B_4C , SiC, and TiC above 1000 °C, *J. Am. Ceram. Soc.* **42**, 300 (1958).
- [66] Z. Zhang and R. M. Wentzcovitch, Anharmonic thermodynamic properties and phase boundary across the postperovskite transition in MgSiO_3 , *Phys. Rev. B* **106**, 054103 (2022).
- [67] B. B. Karki, R. M. Wentzcovitch, S. De Gironcoli, and S. Baroni, First-principles determination of elastic anisotropy and wave velocities of MgO at lower mantle conditions, *Science* **286**, 1705 (1999).
- [68] T. Sun, D. B. Zhang, and R. M. Wentzcovitch, Dynamic stabilization of cubic CaSiO_3 perovskite at high temperatures and pressures from *ab initio* molecular dynamics, *Phys. Rev. B* **89**, 094109 (2014).
- [69] D. B. Zhang, T. Sun, and R. M. Wentzcovitch, Phonon quasi-particles and anharmonic free energy in complex systems, *Phys. Rev. Lett.* **112**, 058501 (2014).
- [70] H. Liu, X. Qian, H. Bao, C. Y. Zhao, and X. Gu, High-temperature phonon transport properties of SnSe from machine-learning interatomic potential, *J. Phys. Condens. Matter* **33**, 405401 (2021).
- [71] Z. Wang, S. Safarkhani, G. Lin, and X. Ruan, Uncertainty quantification of thermal conductivities from equilibrium molecular dynamics simulations, *Int. J. Heat Mass Transf.* **112**, 267 (2017).
- [72] A. J. Chamkha, S. Abbasbandy, A. M. Rashad, and K. Vajravelu, Radiation effects on mixed convection over a wedge embedded in a porous medium filled with a nanofluid, *Transp. Porous Media* **91**, 261 (2012).
- [73] A. Kasaeian, R. Daneshzarian, O. Mahian, L. Kolsi, A. J. Chamkha, S. Wongwises, and I. Pop, Nanofluid flow and heat transfer in porous media: A review of the latest developments, *Int. J. Heat Mass Transf.* **107**, 778 (2017).
- [74] S. Baroni, S. De Gironcoli, A. Dal Corso, and P. Giannozzi, Phonons and related crystal properties from density-functional perturbation theory, *Rev. Mod. Phys.* **73**, 515 (2001).
- [75] A. S. Barker, Jr., Infrared lattice vibrations and dielectric dispersion in corundum, *Phys. Rev.* **132**, 1474 (1963).
- [76] Z. Tong, X. Yang, T. Feng, H. Bao, and X. Ruan, First-principles predictions of temperature-dependent infrared dielectric function of polar materials by including four-phonon scattering and phonon frequency shift, *Phys. Rev. B* **101**, 125416 (2020).
- [77] See Supplemental Material at <http://link.aps.org/supplemental/10.1103/PhysRevB.109.075201> for the scaling law.
- [78] A. F. Ioffe, A. R. Regel, and A. F. Gibson, *Progress in Semiconductors* (Wiley, New York, 1960), Vol. 4.
- [79] Y. Luo, X. Yang, T. Feng, J. Wang, and X. Ruan, Vibrational hierarchy leads to dual-phonon transport in low thermal conductivity crystals, *Nat. Commun.* **11**, 2554 (2020).
- [80] R. S. Krishnan, Raman spectrum of alumina and the luminescence of ruby, *Proc. Indian Acad. Sci.* **26**, 450 (1947).
- [81] K. R. Nagabhushana, B. N. Lakshminarasappa, and F. Singh, Photoluminescence and Raman studies in swift heavy ion irradiated polycrystalline aluminum oxide, *Bull. Mater. Sci.* **32**, 515 (2009).
- [82] S. P. S. Porto and R. S. Krishnan, Raman effect of corundum, *J. Chem. Phys.* **47**, 1009 (1967).
- [83] P. F. McMillan and N. L. Ross, Heat capacity calculations for Al_2O_3 corundum and MgSiO_3 ilmenite, *Phys. Chem. Miner.* **14**, 225 (1987).
- [84] M. R. Querry, *Optical Constants* (US Army Armament, Munitions & Chemical Command, Chemical Research and Development Department, Kansas City, 1985).
- [85] J. Kischkat, S. Peters, B. Gruska, M. Semtsiv, M. Chashnikova, M. Klinkmüller, O. Fedosenko, S. Machulik, A. Aleksandrova, G. Monastyrskiy *et al.*, Mid-infrared optical properties of thin films of aluminum oxide, titanium dioxide, silicon dioxide, aluminum nitride, and silicon nitride, *Appl. Opt.* **51**, 6789 (2012).